Available online at www.sciencedirect.com
ScienceDirect
Global and Planetary Change 53 (2006) 58–77
GLOBAL AND PLANETARY CHANGE
www.elsevier.com/locate/gloplacha

# Millennial-scale variations of sea-ice expansion in the southwestern part of the Okhotsk Sea during the past 120 kyr: Age model and ice-rafted debris in IMAGES Core MD01-2412

Tatsuhiko Sakamoto [a,*], Minoru Ikehara [b], Masao Uchida [c], Kaori Aoki [d], Yasuyuki Shibata [e], Toshiya Kanamatsu [a], Naomi Harada [c], Koichi Iijima [a], Kota Katsuki [f], Hiroshi Asahi [b], Kozo Takahashi [g], Hideo Sakai [h], Hodaka Kawahata [i]

[a] *Institute for Research on Earth Evolution (IFREE), Japan Agency for Marine-Earth Science and Technology (JAMSTEC), Japan*
[b] *Center for Advanced Marine Core Research, Kochi University, Japan*
[c] *Institute of Observational Research for Global Change (IORGC), JAMSTEC, Japan*
[d] *Institute of Geology and Geoinformation, National Institute of Advanced Industrial Science and Technology (AIST), Japan*
[e] *Environmental Chemistry Division, National Institute for Environmental Studies (NIES)-Tandem accelerator for Environmental Research and Radiocarbon (TERRA), Japan*
[f] *Research Center for Coastal Lagoon Environments, Shimane University, Japan*
[g] *Department of Earth and Planetary Sciences, Kyushu University, Japan*
[h] *Department of Earth Science, Toyama University, Japan*
[i] *Ocean Research Institute, University of Tokyo, Japan*

Received 9 September 2004; accepted 20 January 2006

**Abstract**

A 58-m-long sediment core IMAGES MD01-2412 was recovered in the southwestern part of the Okhotsk Sea for high resolution paleoceanography. An age model of the core was obtained by accelerator mass spectrometry (AMS) $^{14}C$ dating of planktonic foraminifer shells, oxygen–isotope stratigraphy of benthic foraminifer calcite, and tephrochronology, resulting in a core-bottom age of 115 kyr. Sea-ice expansion in the Okhotsk Sea was reconstructed by ice-rafted debris (IRD) based on measurement of dropstone, coarse fraction, sand fractions of terrigenous particles, and the magnetic properties. The SW Okhotsk Sea has not had perennial but seasonal sea-ice conditions during the 115 kyr. Seasonal sea ice fluctuated with large amplitudes on millennial scale during the glacials (Marine isotope stage: MIS 2, 3, and 4) and varied relatively little during the Holocene (MIS 1) and the last interglacial (MIS 5). Enhanced polar atmospheric circulation during the glacial resulted in strong wind fields over the Okhotsk Sea and accelerated the large sea-ice expansion during the glacials (MIS 2, 3, and 4). During the interglacials (MIS 1 and 5), sea ice also expanded by small amplitudes. During these periods, decrease of the Amur River discharge would be one of the possible factors for sea-ice expansion. The two main factors of polar atmospheric circulation and Amur River discharge would be responsible for sea-ice expansion during 120 kyr.


*Keywords:* millennial-scale variation; Dansgaard–Oeschger events; Okhotsk Sea; ice-rafted debris; polar atmospheric circulation; Amur River; IMAGES

* Corresponding author. Natsushima-cho 2-15, Yokosuka 237-0061, Japan. Tel.: +81 46 867 9803; fax: +81 46 867 9775.
*E-mail address:* tats-ron@jamstec.go.jp (T. Sakamoto).

0921-8181/$ - see front matter © 2006 Elsevier B.V. All rights reserved.
doi:10.1016/j.gloplacha.2006.01.012

## 1. Introduction

The Okhotsk Sea plays a significant role in climatic and oceanic changes on regional and global scales. The Okhotsk Sea, a far-eastern marginal sea of Eurasia, contains the largest amount of seasonal sea ice in the world. It is the southern limit of sea-ice extent in the northern hemisphere. Sea-ice expansion is sensitive to global warming and cooling in the seasonal sea-ice area. Sea ice is an essential component in climatic and oceanic systems because it regulates exchanges of heat, moisture, and salinity in the surface environment. Once sea ice forms, it affects the regional climate because it has a positive feedback effect on the climatic system due to its high albedo and its inhibitive role on heat transportation between atmosphere and ocean. In particular, seasonal sea ice in the Okhotsk Sea is closely related to winter conditions with cold, strong wind from the Siberia. Very fresh surface water due to discharge from the Amur River also controls the sea-ice extent. In addition, winter convection to greater depths allows sea-ice formation at such low latitudes (Ohshima et al., 2001). Cold dense water is produced by brine rejection during sea-ice formation to form Dense Shelf Water (DSW) in the northern continental shelf regions. The intermediate water in the Okhotsk Sea down to the several hundred meters is much colder, fresher, and richer in dissolved oxygen than that in the North Pacific (e.g., Watanabe and Wakatsuchi, 1998). This Okhotsk Sea Intermediate Water (OSIW) is one of the possible origins of the North Pacific Intermediate Water (Alfulis and Martin, 1987; Talley, 1991). Sea ice and the formation of DSW relate to the OSIW formation. From this point of view, it is very important to elucidate the change of sea ice in the Okhotsk Sea over long timescales for a better understanding of the climatic changes in the high latitudes of the North Pacific.

In order to reveal how the sea-surface environment, including sea-ice coverage, changes and how it relates to the intermediate water formation in the Okhotsk Sea, we focused on the southwestern part of the Okhotsk Sea, where intensive seasonal changes of surface currents are very obvious in the present oceanographic setting. Since the sedimentation rate is estimated to be very high in the area (105 cm/kyr; Kawahata et al., 2003), amplified climatic and oceanographic changes can be reconstructed by sediment–core analyses with a high time resolution. In this paper, we present age model and a record of ice-rafted debris from the sediment core MD01-2412 for the past 120 kyr.

## 2. Modern oceanography in the SW Okhotsk Sea

The major sea-surface-circulation feature of the northern half of the Okhotsk Sea is a cyclonic gyre (Moroshkin, 1966; Ohshima et al., 2002; Itoh et al., 2003) (Fig. 1). Water exchanges between the Okhotsk and the North Pacific mainly through the two deepest straits of the Kuril Straits, the Bussol' Strait (2300 m depth), and the Kuruzenshtern Strait (1900 m depth). The Okhotsk Sea is the site where surface water originating in the North Pacific is modified by mixing with the Amur River water and sea-ice formation, and is transformed into densities that can ventilate to intermediate depths (Itoh et al., 2003). The water-mass transport from the Japan Sea is much smaller than the water-mass exchange with the North Pacific. A southward, cold, and low-salinity current, called the East Sakhalin Current (ESC), flows along the eastern coast of Sakhalin with a typical speed of 20–40 cm/s (Mizuta et al., 2003). Volume transport of the ESC has a maximum of 12 Sv in winter and a minimum of 2 Sv in summer (Ohshima et al., 2001; Mizuta et al., 2003). It reaches the Hokkaido coast in autumn and winter. Surface salinity off Hokkaido drops suddenly <32.0 psu in November or December due to inflow of the ESC (Watanabe, 1963; Akagawa, 1977; Itoh and Ohshima, 2000). The ESC becomes weak and turns to the east toward the Kuril Basin in summer. In the Kuril basin, a weak anticyclonic circulation and mesoscale anticyclonic eddies exist (Wakatsuchi and Martin, 1991; Ohshima et al., 2002).

The southwestern part of the Okhotsk Sea is considered to be a confluence zone of two water masses, the warm and saline Soya Warm Current (SWC) and the cold and fresh ESC (Itoh and Ohshima, 2000). There is an intense seasonal variation of the two sea-surface currents. The SWC originates from the Sea of Japan flowing into the Sea of Okhotsk through the shallow Soya Strait (about 50 m water depth) and flows along the coast of Hokkaido with a width of 40 km and a depth of 0–150 m, which is defined as the water with salinity greater than 33.6 psu (Aota, 1975; Itoh et al., 2003). The SWC is present on the shelf from April to November and achieves maximum velocity in summer and autumn (about 50 cm/s, 1.0 Sv) (Matsuyama et al., 1999). In winter it becomes very weak and intermittent, existing only near the bottom (0–25 cm/s, − 0.3–0.5 Sv) (Aota and Kawamura, 1978; Takizawa, 1982; Itoh and Ohshima, 2000). On the other hand, the cold and less saline ESC originating from the influx of the Amur River dominates the surface layer in November and December (Itoh and Ohshima, 2000; Ohshima et al., 2001).

Sea ice covers about two-thirds of the Okhotsk Sea in winter. Sea ice is brought by both the ESC and the

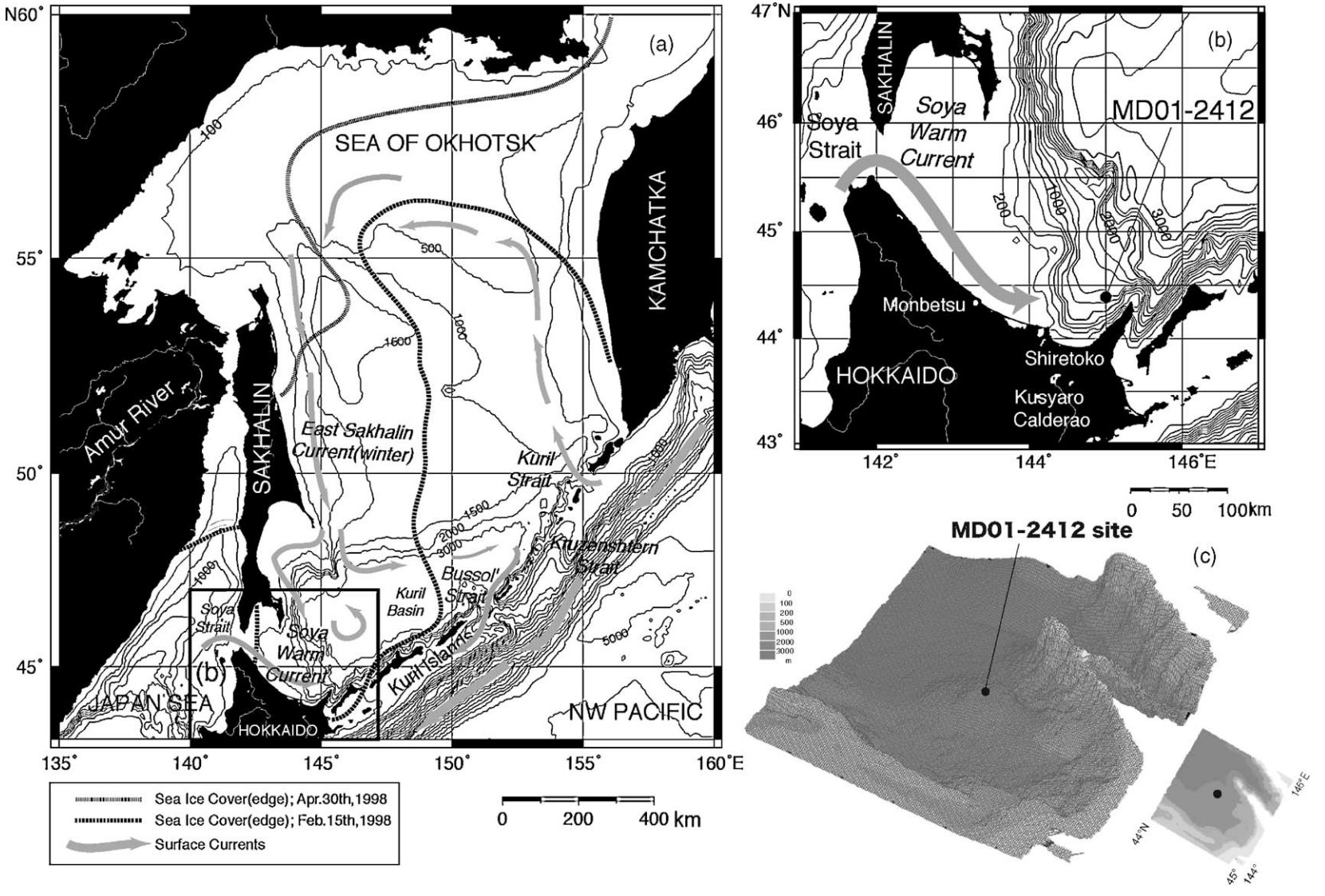


Fig. 1. Location maps of Core MD01-2412 in (a) the whole and (b) the southwestern part of the Okhotsk Sea. The core was corrected at 44°31.657′N and 145°00.25′E, Off Shiretoko Peninsula of Hokkaido Island. Water depth of the core was 1225 m. Extent of sea-ice cover was inferred by sea-ice charts of the Japan Coast Guard (JCD). (c) Bathymetric map around core MD01-2412 site. The map was produced by JODC (Japan Oceanographic Data Center) Data On-line Service System (http://www.jodc.go.jp/service.htm) by using 500 m mesh depth-sounding data. The core was corrected on a little bank on continental slope, Off Shiretoko Peninsula of Hokkaido Island, avoiding direct terrigenous influence.

northerly wind in winter, which makes this region an ice-covered sea in spite of its low latitude (Itoh and Ohshima, 2000). Satellite imagery demonstrates annual variability, both in the extent and in the seasonal expansion of the sea ice (Parkinson et al., 1987; Alfulis and Martin, 1987; Gloerson et al., 1992). It generally covers much of the Okhotsk in March with a thickness of ~ 1 m, but generally retreats by the beginning of June. The sea is usually free of ice for the rest of the year (about 4 months from July to October) (Parkinson et al., 1987). The formation, advance, and retreat of sea ice are influenced by oceanographic and metrological factors, e.g., ice advection and advance can be controlled by wind. Wind conditions and air temperature are both main factors in controlling the inter-annual variation in the maximum sea-ice coverage (Kimura and Wakatsuchi, 1999). Sea ice is mainly formed in the northwestern part of the Okhotsk Sea. Sea ice is generally advected southward by the prevailing northerly or northwesterly winds and is transported by the southward flow of the ESC (Ohshima et al., 2001). The southerly wind transports sea ice that formed in the northern part of the sea toward the south, creating a polynya along the coast that forms new sea ice. In the SW Okhotsk Sea, there is no net production of sea ice (Toyota et al., 2000).

At an intermediate water depth, the Okhotsk Sea has lower salinity and higher oxygen at densities around 26.8 $\sigma_\tau$ (sigma-tau) than any other site in the North Pacific: this is referred to as Okhotsk Sea Intermediate Water (OSIW) (Itoh et al., 2003). The OSIW has a renewal time of 7 yr (Itoh et al., 2003). The OSIW is formed by the mixing of Dense Shelf Water (DSW), the Forerunner of Soya Warm Current Water (FSCW), and Western Subarctic Water (WSAW) (Itoh et al., 2003). Itoh et al. (2003) estimated a mixing ratio among DSW, WSAW, and FSCW as 1:1:0.1 on the assumption of isopycnal mixing. DSW is shelf water at the freezing point with a density of 27.05 $\sigma_\tau$ (sigma-tau) that is formed in the northwest shelf by surface cooling and brine rejection because of sea-ice formation (Kitani, 1973; Itoh et al., 2003). The DSW is thought to be a major ventilation source in the Okhotsk Sea (Kitani, 1973; Alfulis and Martin, 1987). The DSW is transported southward by the ESC (Itoh et al., 2003). The FSCW is the early spring, cold water of the SWC, which is as dense as the OSIW (Takizawa, 1982). Both the FSCW and the DSW have been suggested as the ventilation source for the OSIW (Wakatsuchi and Watanabe, 1998). The OSIW discharged from the Okhotsk Sea joins with warm and saline WSAW in the North Pacific to form the relatively cold and fresh Oyashio Intermediate Water (OYIW) (Itoh et al., 2003). The OYIW is one of the source waters of the NPIW.

## 3. Materials and methods

### 3.1. Sediment core

Core MD01-2412 (44°31.65′N, 145°00.25′E) was collected from the southwestern part of the Okhotsk Sea during Leg 2 of the International Marine Past Global Environmental Changes Study VII (IMAGES; http://www.images-pages.org/) WEPAMA 2001 cruise of the R/V *Marion Dufresne* (Fig. 1). The selected coring site was on a flat bank on the continental slope at a water depth of 1225 m, approximately 100 km north of the Shiretoko Peninsula of Hokkaido where sediment continuously stratifies while avoiding direct terrigenous input of sediment (Fig. 1). A 58.11-m-long sediment core was recovered by the giant piston corer of the R/V *Marion Dufresne* (Fig. 2). The recovered core was divided into 39 sections on shipboard. Shipboard magnetic susceptibility was measured for whole-rounded core. Just after the core was divided, the colors of the sediments were measured by using a spectrophotometer (Minolta CM2022).

The giant piston corer of IMAGES has the great ability of taking a long sediment core up to 60 m; however, it has been reported that the corer produces a significant sediment oversampling and/or stretching of the cores. Széréméta et al. (2004), especially, reported that an oversampling effect was observed in the first 10–18 m of the IMAGES cores. As in the case of core MD01-2412, an obvious stretching effect was observed only in the top 4 m of the section by assessments of the anisotropy of the magnetic susceptibility and the physical properties of the core. The depth of the recovered core was converted from the shipboard depth to a corrected depth by an onshore detailed description that included an assessment of void intervals in the core. The corrected depth of the core was 52.11 m, and this value was used for the age-model construction.

### 3.2. Core lithology

The recovered sediment was composed of homogeneous diatom-bearing silty clay and silty clay with volcanic ash layers (Fig. 2). A major component of the sediments were siliciclastic grains. Microfossils (foraminifera, diatoms) and nannofossils were rare throughout the whole sequence, but diatoms were relatively rich in the sediment in the following intervals of the recovered depth: core-top to 12 m, 27.1 to 31.2 m, 40.4 to 44.0 m, and 46.6 to 52.7 m in shipboard depth. Both slightly and heavily bioturbated intervals were present

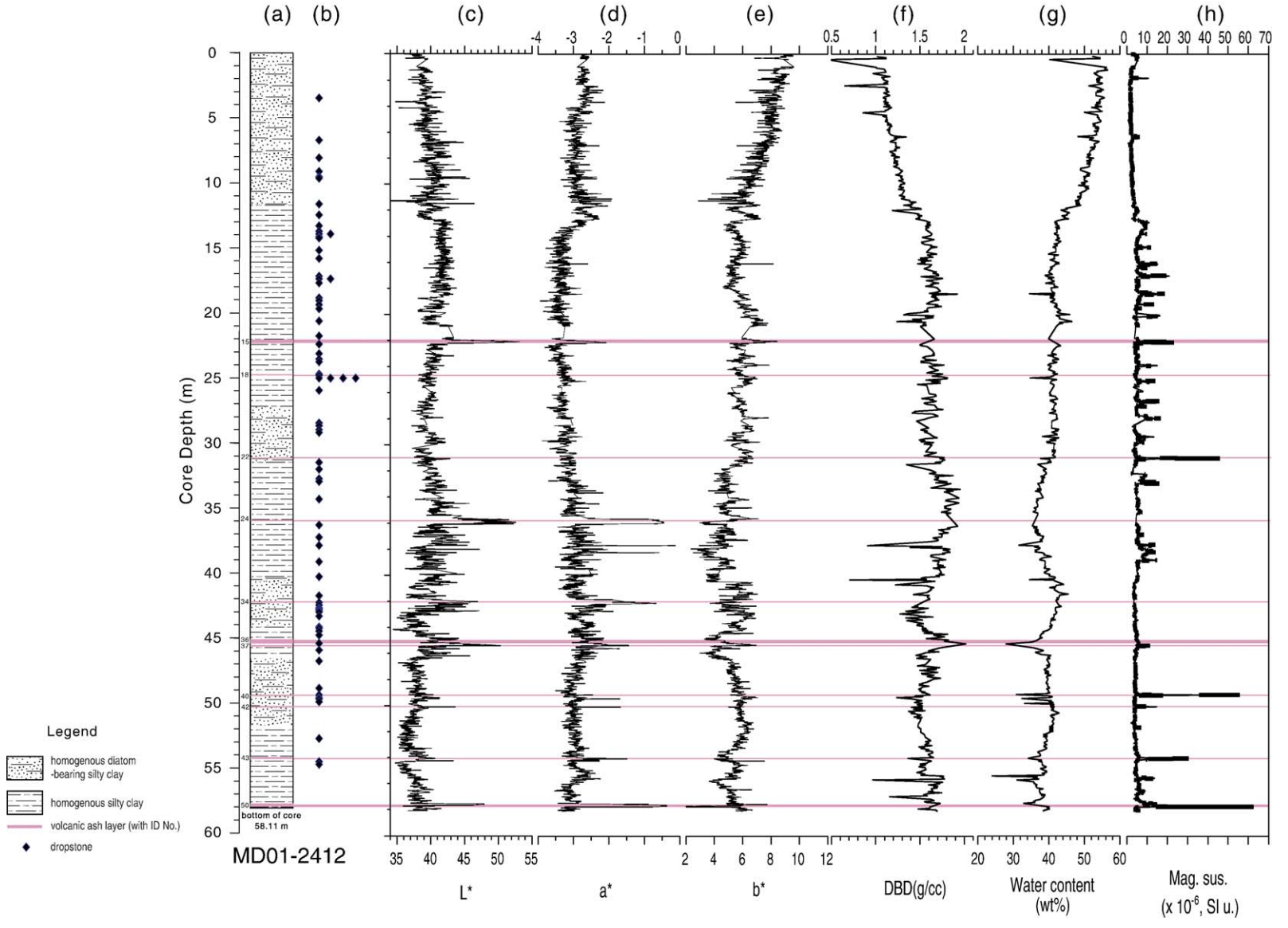


Fig. 2. Columnar core lithology and physical properties of MD01-2412. The core is 58.11-cm long in shipboard depth. (a) Graphic representation of major and minor lithology. MD-12412 consists of homogenous diatom-bearing silty clay and silty clay. Some ash layers were intercalating in silty clay. (b) Occurrence of dropstone, which included shipboard description and recovered samples during off-shored sampling party. Sediment color was shown by (c) $L^*$, (d) $a^*$, and (e) $b^*$. (f) Dry bulk density (DBD), (g) water content, (h) magnetic susceptibility. These physical properties were obtained by offshore measurements.

in the top 13 m and from 33 to 49 m. Eleven obvious tephra layers were recovered in the core, most of which were light grey, light-yellowish grey, or dark grey, thin (1 cm to 3 cm) layers of vitric ash. Three thick (17.2, 12.4, and 13.5 cm) ash layers (Nos. 15, 36, and 50) were also recovered. The ash layers were clearly identified by the peaks of color, density, water content, and magnetic susceptibility (Fig. 2). Magnetic susceptibility of the core increased not only in ash layers but also in other intervals.

The color of the sediment was greyish olive-green throughout the whole core. The $L^*$ and $a^*$ values obviously increased in the ash layers (Fig. 2). The variation of the $b^*$ value corresponded to the variation of the water content in the core, especially in the top 10 m of the core. The intervals of decrease in dry bulk density and the increase in water content corresponded to the intervals of diatom-bearing silty clay.

The sediment often contained dropstone (>2-mm-diameter grains) throughout the core (Fig. 2). Some peaks of magnetic susceptibility corresponded to the occurrence of dropstone, such as about 14 m, 17.5 m, 25 m, 38 m, 49.5 m, and 50 m in shipboard depth.

### 3.3. Magnetic properties measurement

U-channel samples ($2 \times 2$-$cm^2$ cross-section samples) were collected from the working half of the split core sections. Shore-based magnetic susceptibility was measured at 2-cm intervals for the U-channel samples by using a magnetic susceptibility meter (Bartington MS-2). The results were presented in SI units, $10^6/10\ cm^3$. Other magnetic measurements of the U-channels were made at 2-cm intervals using a horizontal cryogenic magnetometer (2-G Enterprises). Natural remnant magnetization (NRM) and demagnetization were routinely measured at the levels of 0, 5, 10, 15, 20, 30, 40, 50, 60, and 70 mT, and, subsequently, anhysteretic remnant magnetization (ARM) was imparted in a 100-mT alternating field (AF) with a 0.1-mT biasing field. ARM was also measured after AF demagnetization of 0, 5, 10, 15, 20, 30, 40, 50, 60, and 70 mT.

### 3.4. Accelerator Mass Spectrometer $^{14}C$ dating

Planktonic foraminifer shells were used for accelerator mass spectrometer (AMS) $^{14}C$ dating. Sediment samples were washed with water and passed through a 63-μm-mesh sieve, and the residual samples on the sieve were dried at 50 °C. Planktonic foraminifer shells of *Neogloboquadrina pachyderma* with test size >125 μm were picked and cleaned with distilled water by an ultrasonicator. Preparation of graphite targets was conducted according to the batch preparation method (Kitagawa et al., 1993). Graphitization of small amounts of carbon, less than 100 μmC, was performed by using the technique modified by National Institute for Environmental Studies-Tandem accelerator for Environmental Research and Radiocarbon Analysis (NIES-TERRA) on the basis of the micro-scale $^{14}C$ analysis developed at National Ocean Sciences Accelerator Mass Spectrometry Facility (NOSAMS) (Pearson et al., 1998; Uchida et al., 2001; Uchida et al., 2004). $^{14}C$ analysis was conducted at the AMS facility of the NIES (Kume et al., 1997; Tanaka et al., 2000). The calendar year (cal yr BP) was calculated from the AMS $^{14}C$ age by using a half-life of 5568 yrs, after calibration of delta $^{13}C$ using CALIB software (Stuiver et al., 1998) for $^{14}C$ ages younger than 24,000 cal yr BP and the calibration equation of Bard et al. (1998) for $^{14}C$ ages older than 24,000 cal yr BP. In this calibration, we assumed that the reservoir effect of $^{14}C$ age in the Okhotsk Sea was 784 ±40 yr (Kuzmin et al., 2001).

### 3.5. Oxygen and carbon isotopes of benthic foraminifera

Sediment samples were washed with water and passed through a 63-μm-mesh sieve, and the residual samples on the sieve were dried at 50 °C. For oxygen and carbon stable isotope analyses, 2–4 specimens of benthic foraminifera, *Uvigerina akitaensis* (>180 μm), were chosen. The samples were slightly crushed and cleaned with ethanol by an ultrasonicator. The cleaned samples were reacted with 100% phosphoric acid for 800 s at 90 °C of equilibrium temperature in a vacuum. The released $CO_2$ was purified and analyzed using an isotope ratio mass spectrometer (IsoPrime, GV Instruments) with better than 0.03‰ analytical precision for the oxygen and carbon isotope ratio of standard NBS-19. The results are expressed according to the Vienna PeeDee Belemnite (VPDB) standard.

### 3.6. Refractive index and chemical composition of tephras

To determine tephrochronology, recovered volcanic origin layers were examined under a stereomicroscope, the refractive indices (RIs) of the volcanic glass and heavy minerals were measured, and the chemical composition of the volcanic glass was analyzed. Samples of tephra were prepared by washing in an ultrasonic cleaner and by recovering the >63 μm size fraction by using a sieve. The volcanic grains in the fraction were separated and classified under a stereomicroscope. The RIs of

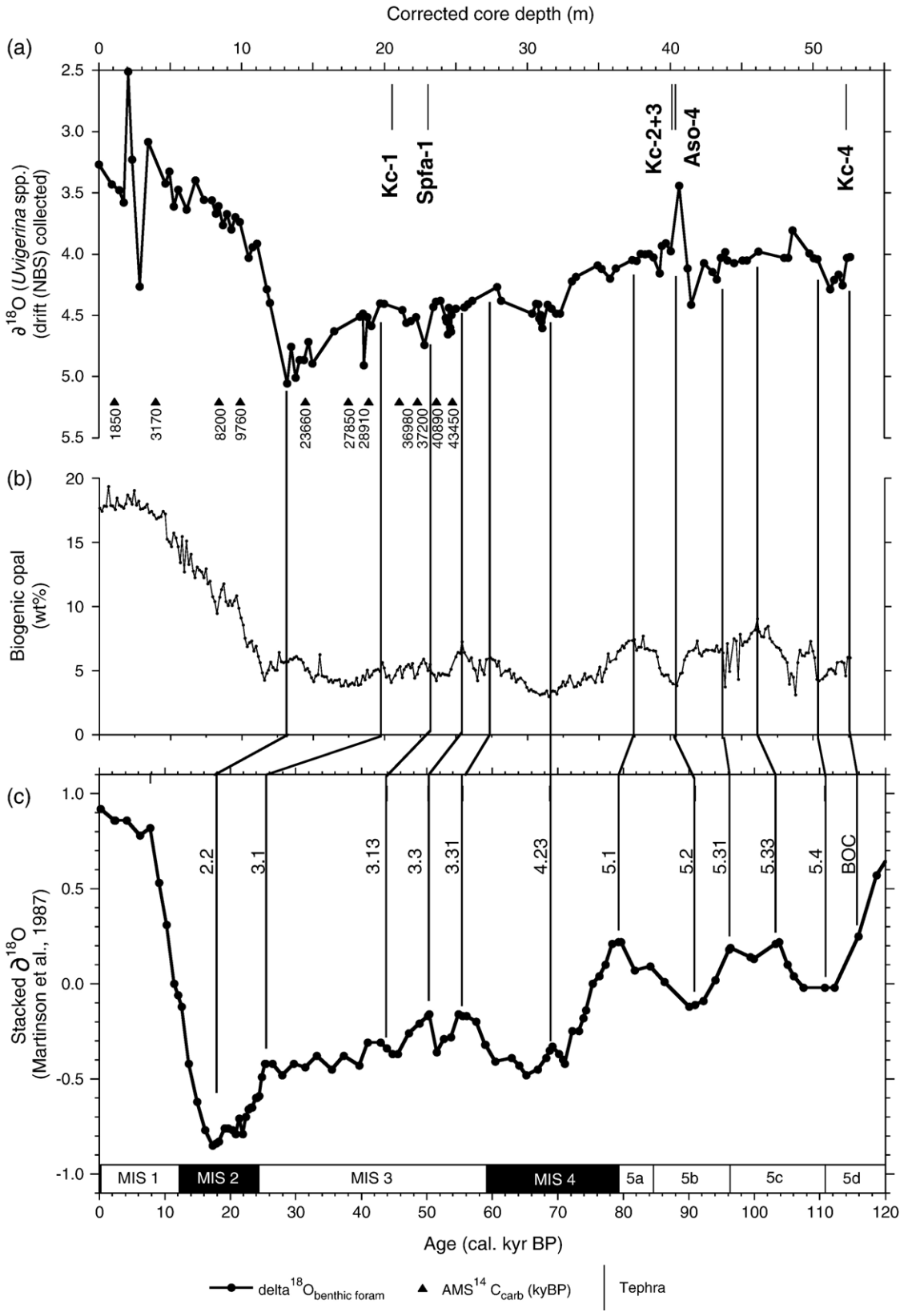
Corrected core depth (m)
(a)
$\partial^{18}O$ (*Uvigerina* spp.) (drift (NBS) collected)
Kc-1
Spfa-1
Kc-2+3
Aso-4
Kc-4
1850
3170
8200
9760
23660
27850
28910
36980
37200
40890
43450
(b)
Biogenic opal (wt%)
(c)
Stacked $\partial^{18}O$ (Martinson et al., 1987)
2.2
3.1
3.13
3.3
3.31
4.23
5.1
5.2
5.31
5.33
5.4
BOC
MIS 1
MIS 2
MIS 3
MIS 4
5a
5b
5c
5d
Age (cal. kyr BP)
delta $^{18}O_{benthic\ foram}$
AMS$^{14}$ $C_{carb}$ (kyBP)
Tephra

Table 1
Results of the Accelerator Mass Spectrometer (AMS) $^{14}C$ dates for planktonic foraminifer in core MD01-2412. All of $^{14}C$ analysis was conducted at the AMS facility of the Tandem accelerator for Environmental Research and Radiocarbon facility of National Institute for Environmental Studies (NIES-TERRA)

| Sample ID | Depth in Core Corrected depth (cm) | Species | Conventional ages (yrs BP) | Error (yrs) | Calendar age (cal yrs BP) |
|---|---|---|---|---|---|
| 2-2A | 107.8 | *N. pachyderma* * | 1880 | 140 | 1850 |
| 4-2A | 398.3 | *N. pachyderma* * | 3750 | 130 | 3170 |
| 7-1(1B,1C,2A) | 840.9 | *N. pachyderma* | 8150 | 110 | 8200 |
| 8-1(1B,1C,2A) | 990.0 | *N. pachyderma* | 9510 | 80 | 9760 |
| 11-2A | 1445.2 | *N. pachyderma* | 20,900 | 350 | 23660 |
| 13-2A | 1745.9 | *N. pachyderma* * | 24,470 | 330 | 27,850 |
| 14-4A | 1888.8 | *N. pachyderma* * | 25,400 | 400 | 28,910 |
| 16-2A | 2102.2 | *N. pachyderma* * | 32,600 | 700 | 36,980 |
| 17-2A | 2230.2 | *N. pachyderma* | 32,800 | 700 | 37,200 |
| 18-1(1B,1C.2A) | 2364.6 | *N. pachyderma* | 36,200 | 460 | 40,890 |
| 19-1((1C,2A) | 2474.9 | *N. pachyderma* | 38,600 | 660 | 43,450 |

* Sample contains <0.2 mg foraminifer.

volcanic glass shards and heavy minerals in each tephra sample were measured by the thermal immersion method as described by Yokoyama and Yamashita (1986) and Danhara et al. (1992), using an RIMS-2000 system (Kyoto Fission Track Co., at Tokyo Metropolitan University). The major element composition of the volcanic glass was analyzed with an electron probe micro-analyzer (EPMA), JXA-8900R (JEOL Co.) operated at 15 kV that used a 10-nA beam current and a 10-μm beam diameter to minimize loss of Na and K (Froggatt, 1983). A counting time of 10 s at the peak was used. The compositions of the glass were calculated as the mean of >20 glass shards.

### 3.7. Biogenic opal analysis

Biogenic opal in aliquot samples was analyzed by a modified chemical technique based on Mortlock and Froelich (1989). Sediment samples were crushed into fine powder after being freeze dried at −45 °C for 24 h. After the samples were dried and crushed, solutions of 10% $H_2O_2$ and 1 N-HCl were added to 20 or 30 mg of the powder in a polypropylene centrifuge tube to remove organic material and calcium carbonate. The biogenic-opal content was determined through extraction using 20.0 ml of a 2M $Na_2CO_3$ solution at 80 °C for 5 h. We verified that the 5-h extraction by the $Na_2CO_3$ solution did not dissolve the volcanic glasses. The biogenic opal was quantified by molybdate-yellow spectrophotometry with a Shimazu UV Mini-1240 Spectrophotometer.

### 3.8. Ice-rafted debris analyses

Three categories of IRD analyses were performed in this study. First, coarse fraction was calculated as weight percent of >63 μm fraction in total fraction. Samples taken by 2.4 cm plastic cube were weighted before and after drying. The samples were washed with water and passed through a 63-μm-mesh sieve, and the residual samples on the sieve were dried at 50 °C and weighted. In this procedure, dry bulk density was calculated. Second, sand-fraction was calculated as the volume ratio of the fraction ranging from 63- to 2000-μm in the total terrigenous fraction based on grain size analysis. The grain-size distribution of terrigenous grains (<2000 μm) was measured in residual solid samples of biogenic opal using a laser diffraction grain-size analyzer (Coulter LS230, at IFREE) with a repeatability of <1% around the mean size. As the repeatability of the instrument depended mainly on proper grain dispersion and the fewest possible air bubbles in the sample chamber, we added to the samples a small amount of sodium hexametaphosphate for dispersion and anhydrous sodium sulfite for eliminating the bubbles. The grain-size analyzer determined the volume % of each size fraction with 133 detectors ranging from 0.04 to 2000 μm in size. Third, the >2000-μm grains (described as dropstone) were picked up and counted recovering number during core-description, sampling, and preparation (Fig. 2).

Fig. 3. Age model of core MD01-2412. (a) Oxygen isotope ratio of *Uvigerina* spp. The ratio was drift (NBS)-corrected. Tied lines showed identified marine oxygen isotope stages (MIS) in this study. Triangles show intervals of AMS $^{14}C$ dates of planktonic foraminifer. Kc-1, Spfa-1, Kc-2/3 (combined ID for Kc-2 and Kc-3), Aso-4, and Kc-4 were identified tephra layers from the Japan arc. Kc: Kucharo caldera, Spfa: Shikotsu caldera, Aso: Aso caldera. (b) Biogenic opal variations in core MD01-2412. (c) Stacked oxygen isotope curve by Martinson et al. (1987) with identified MIS numbers. BOC: bottom of core.

## 4. Results and discussion

### 4.1. Age model for Core MD01-2412

Utilizing AMS $^{14}$C dating of planktonic foraminifer shells, oxygen–isotope stratigraphy for foraminifer calcite, and tephrochronology, we obtained an age model for core MD01-2412.

#### 4.1.1. AMS $^{14}$C dating

First, 11 AMS $^{14}$C dates of the core were determined at the AMS facility of the NIES-TERRA (Fig. 3, Table 1). Radiocarbon ages were converted to calendar-year ages. The radiocarbon age of sample 14-4A, 28,910 cal yr BP, which had contained less foraminifera (<0.2 mg), was not employed in the age model, because the age was much older relative to the $^{14}$C age of adjacent samples.

#### 4.1.2. Oxygen isotope stratigraphy

Second, the marine oxygen isotope stage (MIS) was identified by graphic correlation of oxygen isotope variations of benthic foraminifer, *Uvigerina* spp., in core MD01-2412 to the normalized oxygen–isotope curve of Martinson et al. (1987) (Fig. 3). Biogenic-opal variation in MD01-2412 was used to identify several $\delta^{18}$O events on the assumption of no time lag between biogenic-opal variation and $\delta^{18}$O change. As a result, 11 MIS events, 2.2, 3.1, 3.13, 3.3, 3.31, 4.23, 5.1, 5.2, 5.31, 5.33, and 5.4, were identified in MD01-2412. The ages of MIS 2.2 and 3.1 were consistent with the AMS $^{14}$C dates.

#### 4.1.3. Tephrochronology

Third, tephrochronology was applied to the recovered volcanic origin layers. Five tephras (Kc-1: 30–35 kyr; Spfa-1: 40 kyr; Kc-2/3: 70 kyr; Aso-4: 86–90 kyr; Kc-4: 100–130 kyr) in core MD01-2412 were identified by microscopic observation, measurement of the refractive index, and electron probe X-ray microanalyzer (EPMA) analyses of volcanic glass (Tables 2 and 3). The occurrence of these tephra was consistent with $\delta^{18}$O stratigraphy (Fig. 3). Chemical composition of volcanic glass shards of type tephra on land sections referring for identification of the tephras was listed in Table 3. Tephra No. 15 (Section 15, corrected depth 2046–2063.2 cm) was composed of light grey ash in the lower part and dark grey ash in the upper part of the layer. They contained pumiceous grains and bubble-walled volcanic glasses, including rare orthopyroxene minerals. The RIs of volcanic glass (n) and orthopyroxene ($\gamma$: maximum reflectance) were 1.501–1.504 and 1.705–1.711, respectively. Tephra No. 15 was identified as Kc-1 tephra, which originated from the Kucharo caldera in Hokkaido. Kc-1 was pyroclactic flow

Table 2
List of recovered ash layers and its refractive indices (RI) of volcanic glass and heavy minerals in core MD01-2412. pm: sponge pumice. bw: bubble wall. (y): y-type conjunction of bubble type glass shard. *: colored. fb; fiberous pumice. (y), parenthesis; rare. cpx; clino-pyroxene. opx; ortho-pyroxene. lithic: lithic fragments. ho; hornblende. n; measurement number. The parenthesis in RI column means mode

| Tephra no. | Core | Section | Shipboard depth | | Correction depth | | Thickness (cm) | Description | Max. diameter (μm) |
|---|---|---|---|---|---|---|---|---|---|
| | | | Top (cm) | Bottom (cm) | Top (cm) | Bottom (cm) | | | |
| 15 | MD01-2412 | 15 | 2197.0 | 2211.5 | 2046.0 | 2063.2 | 17.2 | (1) Upper part: dark grey ash<br>(2) Lower part: light grey ash | >250<br>250–1000 |
| 18 | MD01-2412 | 17 | 2477.0 | 2482.0 | 2301.0 | 2306.0 | 5.0 | Light grey, fine ash patches | >250 |
| 22 | MD01-2412 | 21 | 3088.6 | 3095.0 | 2762.5 | 2768.9 | 6.4 | (1) Light grey, pumiceous layers<br>(2) light grey, pumiceous sand layer | 7000 |
| 24 | MD01-2412 | 25 | 3584.0<br>3590.0 | 3586.0<br>3593.5 | 3195.1<br>3201.1 | 3197.1<br>3204.6 | 2.0 | (1) Upper part; ash<br>(2) Lower part: ash | 250–1000 |
| 34 | MD01-2412 | 29 | 4220.0 | 4222.0 | 3723.2 | 3725.2 | 2.0 | Light grey, fine bioturbated ash patches | 1000 |
| 36 | MD01-2412 | 31 | 4539 | 4549 | 4034.2 | 4040.6 | 6.4 | Light grey, fine coarse ash | 250–3000 |
| 37 | MD01-2412 | 31 | 4568.0 | 4571.0 | 4052 | 4054.9 | 2.9 | Light grey, vitric ash | >250 |
| 40 | MD01-2412 | 33 | 4943.0 | 4946.0 | 4410.2 | 4413.2 | 3.0 | Light-yellowish grey, very fine tuffaceous silt | 125–250 |
| 42 | MD01-2412 | 34 | 5015.0 | 5017.0 | 4525.2 | 4527.2 | 2.0 | Light-yellowish grey, coarse-fine ash | 250 |
| 43 | MD01-2412 | 37 | 5416.0 | 5418.0 | 4889.6 | 4891.6 | 2.0 | Yellowish grey, finecoarse ash layers | 500 |
| 50 | MD01-2412 | 39 | 5778.0 | 5791.5 | 5233.0 | 5246.5 | 13.5 | (1) Upper, yellowish ash<br>(2) Lower dark grey ash | |

deposit of the Kucharo caldera. Co-ignimbrite ash of Kc-1 is called as the Kucharo-Shoro (Kc-Sr). The age of this tephra was estimated to be 30–32 kyr (Okumura, 1991; Machida and Arai, 2003). Tephra No. 18 (Section 18, corrected depth 2301–2306 cm) was a 5-cm-thick bioturbated layer of light grey, fine, well-sorted vitric ash. It included bubble-walled volcanic glasses, sponge, and fibrous pumice particles (maximum length of about 2–3 mm), and heavy minerals (1–2 mm) of orthopyroxene and rare hornblende. The RIs of volcanic glass (n) and orthopyroxene ($\gamma$) were 1.501–1.504 and 1.728–1.733, respectively. By its RI, the chemical composition of its volcanic glass, and the high RI value of orthopyroxene, tephra No. 18 was identified as Spfa-1 (Shikotsu pumice fall-1), which is a widespread tephra that came from the Shikotsu caldera in Hokkaido. The age of Spfa-1 was reported as 45 kyr BP (Yanagida, 1994), 39.430±0.56 and 40.120±1.060 kyr BP (Kato et al., 1995) by AMS $^{14}$C dating, and 39.5–40.1 kyr BP by marine oxygen–isotope stratigraphy (Aoki and Arai, 2000). Tephra No. 36 (Section 31, corrected depth 4034.2–4040.6 cm) was a light grey, well-sorted, fine to coarse, vitric ash layer, containing bubble-walled volcanic glass shards, 2- to 3-mm-diameter pumiceous grains, and the heavy minerals of ortho- and clino-pyroxene. The RIs of the volcanic glass (n) and orthopyroxene ($\gamma$) were 1.505–1.509 (mode was 1.505–1.507) and 1.707–1.711, respectively. The tephra was identified as Kc-2/3 pyroclastic flow deposits, which originated from the Kucharo caldera in Hokkaido by the RI and the chemical composition of volcanic glass. The age of Kc-2/3 (Kc-2 and Kc-3) was estimated roughly to be 70 kyr (Machida and Arai, 2003). Tephra No. 37 (Section 31, corrected depth 4052–4054.9 cm) was light grey, well-sorted, fine, and vitric ash that was recovered from a 3-cm-thick layer. It included abundant volcanic glass shards and rare phenocryst minerals, orthopyroxene, and hornblende. The RIs of the volcanic glass ($n$), orthopyroxene ($\gamma$), and hornblende ($n_2$) were 1.505–1.510, 1.699–1.701, and 1.685–1.693, respectively. Tephra No. 37, identified as Aso-4 tephra, which was widespread all over the Japanese islands, came from the Aso caldera in Kyushu, Japan (Machida and Arai, 2003; Aoki and Arai, 2000). The Aso-4 is known to be identical because it has an extremely high RI of hornblende and a low RI of clino-pyroxene compared with other tephra in Japan. The age of Aso-4 was estimated to be 86–90 kyr (Machida and Arai, 2003). Tephra No. 50 (Section 39, corrected depth 5233–5246.5 cm) was a 13.5-cm-thick layer of lower dark-grey ash and upper yellowish-grey ash. It was a well-sorted, fine vitric ash layer that included non-colored and colored pumiceous

| Volcanic glass type | Minerals | | | Refractive index | | Identification |
|---|---|---|---|---|---|---|
| | 125–250 (μm) | 63–125 (μm) | Glass ($n$) | Orthphroxene ($\gamma$) | Hornblende ($n_2$) | |
| pm, bw(y), (pm*, bw*) | (cpx) | – | – | – | – | Kc-1 |
| – | – | – | 1.501–1.504 | 1.706–1.711 | – | |
| pm, fb, bw | – | – | 1.501–1.504 (1.502–1.503) | 1.728–1.733 ($n$=7) | rare | Spfa-1 |
| – | – | – | – | – | – | Not specified |
| pm | opx,cpx | ho,cum? | 1.502–1.506 | 1.703–1.712 | rare | Reworked? |
| – | – | – | – | – | – | Not specified |
| pm, fb | opx,cpx | – | 1.505–1.506 | – | – | |
| pm, (pm*,bw*,ob) | opx,cpx | – | 1.503–1.505;1.509–1.512 | – | – | Not specified |
| pm, bw,(ob) | opx,cpx | – | 1.505–1.509 (1.505–1.507) | 1.707–1.711 | – | Kc-2/3 |
| | – | – | 1.506–1.510 | 1.699–1.701 ($n$=5) | 1.686–1.693 ($n$=9) | Aso-4 |
| pm, bw, (bw*) | lithic | – | 1.506–1.511 | – | – | Not specified, reworked |
| pm, (pm*) | lithic | – | 1.512–1.515(over 1.515) | – | – | Not specified, reworked |
| pm, pm* | opx,cpx | – | >1.515 | – | – | Not specified |
| | – | – | 1.503–1.506 | – | – | Kc-4 |
| pm, bw, (pm*) | lithic, opx, cpx | – | 1.502–1.506 | 1.706–1.710($n$=18) | Present | |

Table 3
Results of major chemical composition of volcanic glass in recovered ash layers in core MD01-2412 and type tephra erupted from volcanoes in the Hokkaido islands, Japan. *n*: number of measurement. FeO*: total iron. 1): Machida and Arai (2003). 2): Takahashi et al. (2004)

| Tephra no. | Tephra identification | Core | Section | Shipbpard depth (cm) | | Corrected depth (cm) | | $SiO_2$ (wt.%) | $TiO_2$ (wt.%) | $Al_2O_3$ (wt.%) |
|---|---|---|---|---|---|---|---|---|---|---|
| | | | | Top | Bottom | Top | Bottom | | | |
| No.15 | Kc-1 | MD01-2412 | 15 | 2197.0 | 2211.5 | 2046.0 | 2063.2 | 78.23 (0.40) | 0.26 (0.10) | 12.13 (0.20) |
| No.18 | Spfa-1 | MD01-2412 | 17 | 2477.0 | 2482.0 | 2301.0 | 2306.0 | 77.90 (0.20) | 0.14 (0.10) | 12.29 (0.10) |
| No. 36 | Kc-2/3 | MD01-2412 | 31 | 4039 | 4549 | 4034.2 | 4040.6 | 77.05 (1.00) | 0.32 (0.10) | 12.66 (0.40) |
| No. 37 | Aso-4 | MD01-2412 | 31 | 4568.0 | 4571 | 4052 | 4054.9 | 72.08 (0.60) | 0.39 (0.10) | 14.78 (0.30) |
| No. 50 | Kc-4 | MD01-2412 | 39 | 5778.0 | 5791.5 | 5233.0 | 5246.5 | 77.97(0.90) | 0.31 (0.10) | 12.08 (0.60) |
| | Tephra Name | Sampling site | | | | | | $SiO_2$ (wt.%) | $TiO_2$ (wt.%) | $Al_2O_3$ (wt.%) |
| Reference | Kc-1 (co-ignimbrite) | Shoro[1)] | | | | | | 78.52 (0.40) | 0.26 (0.04) | 12.14 (0.19) |
| Reference | Spfl (pfl) | Tomakomai[1)] | | | | | | 78.56 (0.50) | 0.15 (0.05) | 12.45 (0.31) |
| Reference | Spfa-1 (afa) | Kamisarabetsu[1)] | | | | | | 77.99 (0.49) | 0.15 (0.04) | 12.53 (0.24) |
| Reference | Spfa-1 (afa) | Shirataki[2)] | | | | | | 78.55 (0.31) | 0.14 (0.03) | 12.16 (0.11) |
| Reference | Kc-2/3 (pfl) | Higashikayano[1)] | | | | | | 77.54 (1.91) | 0.35 (0.16) | 12.67 (0.54) |
| Reference | Aso-4 (co-ignimgrite) | Onnenai[1)] | | | | | | 72.30 (0.55) | 0.41 (0.12) | 14.74 (0.28) |
| Reference | Kc-4 (pfl) | Nakasyari[1)] | | | | | | 78.32 (0.55) | 0.33 (0.05) | 12.07 (0.28) |

grains and bubble-walled volcanic glass. Ortho- and clinopyroxene were included and hornblende was present in the layers. The RIs of volcanic glass (n) and orthopyroxene (γ) were 1.502–1.506 and 1.706–1.710, respectively. Tephra No. 50 was identified as Kc-4 tephra, which was a volcanic ash layer accompanied with the fourth and the largest pyroclastic flow of the Kucharo caldera. Co-ignimbrite ash of Kc-4 is called as the Kucharo-Haboro (Kc-Hb) tephra. The age of the Kc-4 was not well determined but it was estimated to be 100–130 kyr (5e–5d transition) by comparison with land sections (Machida and Arai, 2003). Even though its stratigraphic level was consistent with radiocarbon ages and oxygen isotope stratigraphy, tephra Spfa-1 was rejected in constructing the age model because there was a peculiarly high sedimentation rate with a radiocarbon age of 40.890 kyr at the intervals just below Spfa-1. The age of tephra Kc-2/3 was also not used in the age model because it was just above the well-dated Aso-4 tephra.

#### 4.1.4. Age model and sedimentation rate

Consequently, we have constructed an age model for core MD01-2412 by adopting 20 time-control points (Fig. 4a, Table 4), including nine AMS $^{14}C$ data, seven oxygen–isotope events, and three tephra intervals. The age of the core bottom was calculated to be 115,910 yr by correlation of oxygen–isotope curves concordant with the Kc-4 age. The average sedimentation rate was as high as 115.5 cm/kyr during the Holocene and as low as 41.2 cm/kyr during glacials (Fig. 4b). The estimated sedimentation rate of ~ 115.5 cm/kyr during the Holocene was consistent with 105 cm/kyr for the Holocene core HO76 from SW Okhotsk (Kawahata et al., 2003). An abnormally high sedimentation rate of 220.11 cm/kyr between 107.8 and 398.3 m was considered to be artificial, a result of core expansion in the top 4 m of the core. If we were to apply the average sedimentation rate of 91.78 cm/kyr between 398.3 and 990 cm to the interval from 107.8 and 398.3 cm, the top part of the core should be expanded by 2.4 times from its original length. The sedimentation rate in the interval from the core top to 107.8-cm depth was calculated to be as low as 58.24 cm/kyr. If the same 91.78 cm/kyr would apply to intervals from the core top to 107.8 cm, the age of the core top would be calculated as 675 yr. This would mean that 62 cm of the core top had been lost by coring. Nevertheless, we assumed a core-top age of 0 kyr in the age model in this study.

#### 4.1.5. Identification of Dansgaard–Oeschger events

Rapid warming events on a millennial timescale in Core MD01-2412, including the DO cycles and the Younger Dryas (YD) and Bølling–Ållerød (B/Å) events, were identified in an alkenone-derived sea surface temperature (alkenone SST) record (Harada et al., 2006-this volume) by graphical correlation with the

| FeO* (wt.%) | MnO (wt.%) | MgO (wt.%) | CaO (wt.%) | $Na_2O$ (wt.%) | $K_2O$ (wt.%) | *n* | Total (wt.%) |
|---|---|---|---|---|---|---|---|
| 1.53 (0.10) | 0.07 (0.00) | 0.28 (0.00) | 1.51 (0.10) | 3.51 (0.30) | 2.48 (0.10) | 29 | 98.12 (1.30) |
| 1.63 (0.10) | 0.07 (0.10) | 0.16 (0.00) | 1.43 (0.00) | 3.69 (0.00) | 2.71 (0.10) | 30 | 97.36 (1.40) |
| 1.86 (0.30) | 0.08 (0.00) | 0.35 (0.10) | 1.69 (0.20) | 3.92 (0.20) | 2.07 (0.10) | 40 | 95.77 (1.50) |
| 1.74 (0.20) | 0.09 (0.00) | 0.39 (0.10) | 1.18 (0.20) | 4.37 (0.20) | 4.99 (0.20) | 20 | 97.51 (1.00) |
| 1.69 (0.20) | 0.09 (0.10) | 0.29 (0.10) | 1.46 (0.30) | 4.00 (0.20) | 2.09 (0.50) | 35 | 96.01 (1.30) |
| FeO* (wt.%) | MnO (wt.%) | MgO (wt.%) | CaO (wt.%) | $Na_2O$ (wt.%) | $K_2O$ (wt.%) | n | Total (wt.%) |
| 1.33 (0.14) | 0.07 (0.03) | 0.25 (0.03) | 1.34 (0.08) | 3.69 (0.13) | 2.40 (0.08) | 21 | 97.85 (1.21) |
| 1.37 (0.12) | 0.05 (0.04) | 0.13 (0.02) | 1.23 (0.05) | 3.41 (0.14) | 2.64 (0.09) | 21 | 98.10 (1.98) |
| 1.47 (0.11) | 0.08 (0.04) | 0.13 (0.03) | 1.30 (0.04) | 3.78 (0.24) | 2.58 (0.08) | 23 | 93.03 (1.36) |
| 1.69 (0.12) | 0.04 (0.02) | 0.13 (0.02) | 1.18 (0.04) | 3.69 (0.24) | 2.42 (0.06) | 16 | 97.63 (1.37) |
| 1.81 (0.66) | 0.08 (0.04) | 0.32 (0.16) | 1.63 (0.47) | 3.77 (0.24) | 1.83 (0.08) | 18 | 96.56 (1.14) |
| 1.74 (0.18) | 0.10 (0.03) | 0.38 (0.07) | 1.15 (0.18) | 4.14 (0.15) | 5.04 (0.21) | 33 | 95.80 (1.24) |
| 1.49 (0.15) | 0.11 (0.05) | 0.23 (0.02) | 1.29 (0.08) | 4.14 (0.12) | 2.02 (0.07) | 17 | 97.95 (1.65) |

GISP2 ice-core oxygen isotope change (Dansgaard et al., 1993; Steiget et al., 1994; White et al., 1997; Stuiver et al., 1995). On the basis of the age model of the core, the average time resolution of a sample for alkenone measurement was calculated to be about 100 yr during glacial periods and about 20 yr during the Holocene. Thus, the alkenone SST record was considered to be sufficient to correlate with the GISP2 record. In the comparison of the alkenone SST record of core MD01-2412 with the GISP2 $\delta^{18}O$ record, only some warm events (interstadials 2, 12, 13, 17, 18, and 19) could not be clearly identified in the alkenone SST record in core MD01-2412. Clearly seen in the alkenone data are a very warm B/Å, strong H1 (Heinrich event), and a general trend of warming through MIS. The age of the identified DO events in core MD01-2412 was not tuned to the GISP2 timescale in this study, although most of the interstadial events were identified in the core.

### 4.2. Sea-ice related proxies

#### 4.2.1. Magnetic susceptibility and ARM30/ARM ratio

Volume magnetic susceptibility is generally considered to be a quantitative measurement of ferromagnetic mineral concentration in the sediment. The source grains include not only ferromagnetic minerals but also other kinds of siliciclastic minerals that have magnetic fabrics. Magnetic susceptibility of U-channel samples from Core MD01-2412 shows obvious variation in time domain (Fig. 5a). 53 peaks of magnetic susceptibility were identified during 120 kyrs (M1 to M53). There are more peaks during the glacial periods (MIS 2, 3, and 4) than the interglacial periods (MIS 1 and 5). By stereoscopic observation for grain containing in the intervals of all peaks of magnetic susceptibility, peaks consisted of various colored, coarse- and sand-sized, sub-angular to angular fragments of igneous and sedimentary rocks with a few volcanic grains. These peaks are identified not to be volcanic origin intervals. Based on core description (Fig. 2 and Table 2), peaks of M20, M24, M35, M38, M45, M46, M47, M49, and M52 correspond to volcanic ash and pumiceous layers. Relative low value of magnetic susceptibility of M24 and M45, corresponding Spfa-1 and Kc-2/3 tephra layers, results from low recovery of those layers in U-channel samples. Another thin ash layer (assigned as Mx in Fig. 5a) is identified during core description, however, there is no obvious peak of magnetic susceptibility.

The volume magnetic susceptibility also depends on the grain-size of magnetic minerals (Mahar, 1988; Kanamatsu and Matsuo, 2003). The sediment may include various sizes of ferromagnetic minerals and different kinds of magnetic sources. The ARM30/ARM ratio (ARM30 = residual ARM after AF cleaning at 30 mT) can be used to assess a parameter that strongly depends on the grain size of the magnetic grains. In general, an increase of the ARM30/ARM ratio is relatively the result of rich

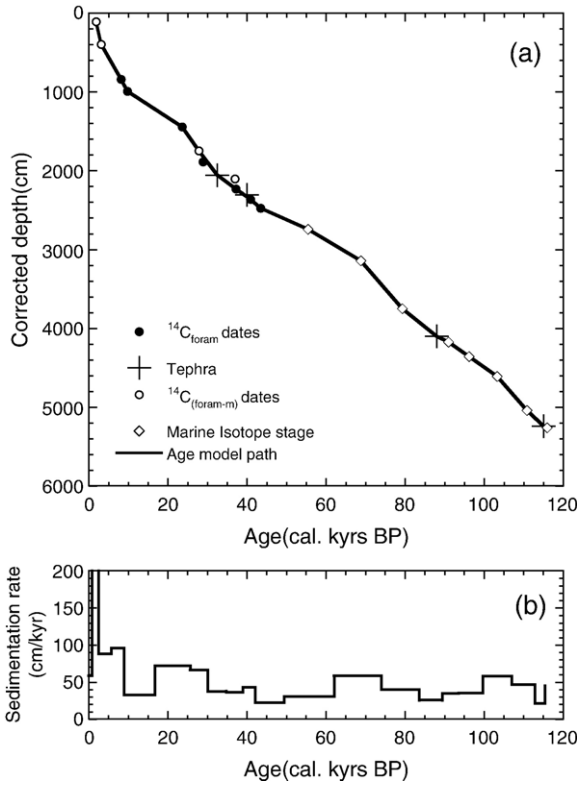


Fig. 4. Depth–age plot (a) and sedimentation rate (b) of MD01-2412 by adopting 20 time-control points. The radiocarbon age of 28,910 cal yr BP, which contained less foraminifer (<0.2 mg), the tephra Spfa-1 (corrected depth 2301—2306 cm), and tephra Kc-2/3 (corrected depth 4034.2–4040.6 cm) were not employed in the age model. An abnormally high sedimentation rate of 220.11 cm/kyr between 107.8 and 398.3 m was considered to be artificial by core expansion in the top 4 m of the core.

small grains of ferromagnetic minerals and vice versa. The ARM30/ARM ratio of Core MD012412 shows approximately constant value about 0.55 during early MIS1, late MIS2, MIS4, and MIS5 (Fig. 5f) with high frequency variation. Peaks of magnetic susceptibility always correspond to either peaks or troughs of the ARM30/ARM ratio (Fig. 5a and f), suggesting different grain sizes of magnetic minerals are included within dropstone, coarse, and fine grains in the sediments. Several high values of the ratio are often found during early MIS2 and MIS3. It is implying grains size of magnetic minerals during cold intervals become finer than other periods by enhanced vertical convection, coastal suspension freezing, and grounding of sea-ice near coastline on continental shelf with low sea-level stand.

### *4.2.2. Coarse fraction*

Coarse fraction, which is the residual on the 63 μm sieve, is mainly composed of terrigenous grains including various lithic fragments of igneous and sedimentary rocks, individual grains of quartz, feldspar, hornblende, pyroxene, and magnetite. Volcanic grains of glass shards and pumiceous fragments are also included in coarse fraction, however, amount of those are small excepting obvious ash and pumiceous layers. It includes very few biogenic fractions throughout the core by the stereoscopic observation, predominantly consisting of planktonic and benthic foraminifera in coarse fraction. As total range of coarse fraction in bulk samples is ranging from 1.6% to 35.4 wt.% (Fig. 5c), biogenic fraction is small, ranging from 0.06% to 0.12% in coarse fraction. In this study, the value of coarse fraction is, therefore, regarded as almost terrigenous because biogenic component in coarse fraction is almost negligible in full range of the variation.

Coarse fraction varies in time with the average of ~ 1.1 wt.% with high frequency variation (Fig. 5c). The variation in mass accumulation rate (AR) of coarse fraction does not show much difference from that in weight %. The AR strongly correlate with high sedimentation rate during MIS 2, late MIS3, and MIS4. In both measurement units, the peaks of coarse fraction always corresponds to peaks of magnetic susceptibility, except for five small peaks of coarse fraction and clear peaks at the intervals of volcanic origin layers (M35,

Table 4
Time control points for age model of core MD01-2412. Core-top was assumed 0 m at sea bottom and 0 yrs BP in this age model. SR: Sedimentation Rate. AMS: Accelerator Mass Spectrometer. MIS: marine isotope stage. BOC: bottom of core

| Core | Section | Sample ID | Depth in core corrected depth (cm) | Age (yrs BP) | SR (cm/kyrs) | Methods |
|---|---|---|---|---|---|---|
| MD01-2412 | Core-top | – | 0.0 | 0 | 58.24 | |
| MD01-2412 | 2 | 2A | 107.8 | 1850 | 220.11 | AMS$^{14}$C |
| MD01-2412 | 4 | 2A | 398.3 | 3170 | 87.99 | AMS$^{14}$C |
| MD01-2412 | 7 | 1B+1C+2A | 840.9 | 8200 | 95.58 | AMS$^{14}$C |
| MD01-2412 | 8 | 1B+1C+2A | 990.0 | 9760 | 32.75 | AMS$^{14}$C |
| MD01-2412 | 11 | 2A | 1445.2 | 23,660 | 71.77 | AMS$^{14}$C |
| MD01-2412 | 13 | 2A | 1745.9 | 27,850 | 66.39 | AMS$^{14}$C |
| MD01-2412 | 15 | – | 2054.6 | 32,500 | 37.36 | Tephra(Kc-1) |
| MD01-2412 | 17 | 2A | 2230.2 | 37,200 | 36.42 | AMS$^{14}$C |
| MD01-2412 | 18 | 1B+1C+2A | 2364.6 | 40,890 | 43.09 | AMS$^{14}$C |
| MD01-2412 | 19 | 1C+2A | 2474.9 | 43,450 | 22.20 | AMS$^{14}$C |
| MD01-2412 | 21 | 4C | 2741.3 | 55,450 | 30.09 | MIS 3.31 |
| MD01-2412 | 24 | 12A | 3143.9 | 68,830 | 58.13 | MIS 4.23 |
| MD01-2412 | 29 | 4C | 3749.7 | 79,250 | 40.10 | MIS 5.1 |
| MD01-2412 | 31 | – | 4053.5 | 88,000 | 25.49 | Tephra (Aso-4) |
| MD01-2412 | 32 | 6C | 4175.7 | 90,950 | 34.57 | MIS 5.2 |
| MD01-2412 | 33 | 13A | 4357.6 | 96,210 | 35.55 | MIS 5.31 |
| MD01-2412 | 35 | 5C | 4609.3 | 103,290 | 57.93 | MIS 5.33 |
| MD01-2412 | 38 | 2C | 5043.7 | 110,790 | 46.57 | MIS 5.4 |
| MD01-2412 | 39 | – | 5239.8 | 115,000 | 21.32 | Tephra (Kc-4) |
| MD01-2412 | 39 | 11C | 5259.2 | 115,910 | | BOC |

Mx, M45, M46, M47, M49, and M52). The five small peaks (marked with *a** in Fig. 5c) consist of dark-colored coarse lithic fragments with a few pumiceous grains that may non-magnetic grains. Distinct peaks of coarse fraction at M16 contain sub-rounded brown-colored pumiceous grains in coarser part of the fraction, implying not volcanic layer. On the other hand, the fraction at peaks of volcanic origin layers, for instance, M46 and M47 contains rich large fragment of volcanic glass and pure pumiceous grains, respectively. 11 peaks of coarse fraction correspond to decreasing intervals of ARM30/ARM (M1, M3, M9, M17, M18, M19, M23, M37, M42, M48, and M51). In the seasonal sea-ice area, sea-ice rafting is only a mechanism for transferring more than several μm grains into hemi-pelagic environment. Although the coarse fraction estimation in this study includes sand-sized fraction, except for volcanic layers, it is regarded as ice-rafted debris.

*4.2.3. Grain size distribution and sand fraction*

A grain-size distribution of the terrigenous fraction ranging from 0.04 to 2000 μm after removal of organic carbon, biogenic carbonate, and biogenic silica from bulk samples was typically divided into three types. The first type was a silt-rich single modal distribution that was abundant in the Holocene samples (Fig. 6a). The silt peak centered at 30 μm in diameter in the figure varied among samples. The second type was a bimodal distribution, which had two modes peaked at around 6 μm and 115 μm in diameter (Fig. 6a). This silt and sand bimodal distribution occurred mainly in glacial samples. Obvious troughs in the grain-size distributions of glacial samples are 28 and 63 μm in diameter. The third distribution type was the richest in sand among the three types (Fig. 6c), being a bimodal distribution. The sand fraction in this type was richer than the clay and silt fractions. The modes of the sand fraction peaked at around 90–100 μm. The trough in the grain-size distribution in this type was centered at 28 μm in diameter. This type was found almost always in stadial samples. Distinct grain size distributions of sand-sized particles in bimodal distribution of glacial and stadial samples suggest a physical transportation by ice rafting with ocean current transportation of clay and silt-sized particles.

The sand fraction in the second and the third types of grain size distribution consisted of sub-round, sub-angular, or angular grains of transparent and reddish colored quartz, feldspars, hornblende, pyroxene, colored and non-colored pumice, scoria, magnetite, chart, and lithic fragments under stereoscope (Fig. 6d). On the basis of the distinct grain-size distribution, the sand-fraction content was calculated in this study as the volume ratio of the fraction ranging from 63- to 2000-μm in the total terrigenous fraction.

Obvious increasing interval of sand fraction is found during MIS 2 (Fig. 5e). The interval corresponds to broad increase of volume magnetic susceptibility

including peaks of M8, M9, and M10 where coarse fraction does not increase so much. During the MIS3, sand fraction increases several times, corresponding to peaks of volume magnetic susceptibility and increasing intervals of the ratio of ARM30/ARM such as M13, M22, M25, M30, M31, and M32).

#### 4.2.4. Dropstones

Dropstones were recovered throughout the core during not only glacial but also interglacial (Fig. 5b). The diameter of recovered dropstones ranged from 2 to 28 mm, averaging 7 mm for the maximum axis. It consisted of various colored, sub-angular to angular fragments of igneous rocks, volcanic scoria, and sedimentary rocks. Some peaks of magnetic susceptibility corresponded to the occurrence of dropstone. The dropstone was rich during the peaks of sand fraction, but it was also observed during intervals of low sand-fraction concentration. Occurrence of dropstone often corresponded to the peaks of magnetic susceptibility. It is, however, not a simple linear relation between dropstone and magnetic susceptibility because the occurrence of the dropstone strongly depended on a chance to find during sampling, therefore, recovery of it was not quantitative measurement. Anyhow, only a mechanism transferring grains of >2 mm-diameter into hemi-pelagic environment is ice drifting especially in seasonal sea-ice area.

### 4.3. Modern ice-rafting process and the past sea-ice proxies

#### 4.3.1. Modern sea-ice formation

In the present, sea-ice in the Okhotsk Sea is mostly formed in the northwestern part of the Okhotsk Sea. A strong wind field during winter is affected by the development of the Aleutian Low over the Okhotsk region expanding the sea-ice cover in the Okhotsk Sea (Kimura and Wakatsuchi, 1999). Sea-ice is drifted southward by northerly or northwesterly winds and by the southward flow of the ESC (Ohshima et al., 2001). As sea-ice drifts southward, the southerly wind creates a polynya along the coast resulting in the formation of new sea-ice. In the SW Okhotsk Sea, there is no net production of sea ice (Toyota et al., 2000); therefore, the source of sea-ice is only from the north, delivered by strong ESC during winter. During sea-ice formation and drifting, terrigenous clastic grains are incorporated into sea-ice mainly through coastal suspension freezing and when the sea-ice is grounded near coastline on continental shelf. The grains are subsequently transported far away from land to the open sea by drifting sea-ice. In the Okhotsk Sea, the content of the IRD in surface sediment is related to the sea-ice extent (Sakamoto et al., 2005). The spatial distribution of IRD in surface sediments closely corresponded to the average sea-ice extent in the winter.

#### 4.3.2. Modern ice-rafting process

Previous sediment-trap experiments on the eastern shelf of the Sakhalin Islands revealed processes involved in present-day IRD sedimentation that showed that a distinct sand-sized fraction was a product of spring IRD flux during sea-ice melting (Sakamoto et al., 2005). It is evident that seasonal IRD, consisting mainly of angular sand-sized particles, were released just after sea-ice melting in spring. These modern observations confirmed that sea-ice in the Okhotsk Sea captured terrigenous grains when it formed in the NW part of the Okhotsk Sea and/or when sea-ice became grounded near the coastline on the continental shelf during southward drifting, and that sea-ice released the grains to the sea bottom when it melted. The IRD in the Okhotsk Sea, at least in the western part of the sea, consist of a series of grains of >63 μm diameter in size.

#### 4.3.3. Sea-ice proxies of the past SW Okhotsk Sea

In the sediment core, magnetic susceptibility increases in most of the intervals where both coarse and sand fraction increase (green tie lines in Fig. 5) and in 5 intervals where either coarse or sand fractions increase (blue tie lines in Fig. 5), although the measurement unit is different between coarse (wt.%) and sand fraction (vol.%). Occurrence of dropstone often corresponds to the peaks of magnetic susceptibility.

Ice rafting is the only the mechanism for transferring dropstone and coarse fraction into hemi-pelagic sea floor in seasonal sea-ice area. Variations in sand

Fig. 5. Sea-ice related proxies in Core MD01-2412 in the SW Okhotsk. Tied lines in this figure were intervals of obvious peaks of magnetic susceptibility. (a) Volume magnetic susceptibility measured at 2 cm intervals for U-channel samples. M-raveled numbers represents identified peaks of magnetic susceptibility. (b) Occurrence of dropstone recovered during core-description, sampling, and preparation. The dot shows an interval of occurrence. (c) Coarse fraction (>63 μm in grain size) in weight %. The symbol (*) represents small peaks of coarse fraction that do not have obvious to peaks of magnetic susceptibility. (d) Coarse fraction (>63 μm in grain size) in accumulation rate (AR) (g/cm$^2$/kyr). (e) Sand fraction (63–2000 μm) in volume %. (f) Anhysteretic remanent magnetization (ARM). Value of ARM 30/ARM means value of ARM measured after AF demagnetization of 30 mT was divided by value of ARM imparted in a 100-mT alternating field (AF) with a 0.1-mT biasing field. (g) Relative abundance of diatom sea-ice algae, *Fragilariopsis cylindrus* (Okazaki et al., 2005). (h) Stacked oxygen isotope curve by Martinson et al. (1987) and oxygen isotope ratio of *Uvigerina* spp. The ratio was drift (NBS)-corrected. MIS=marine isotope stage.

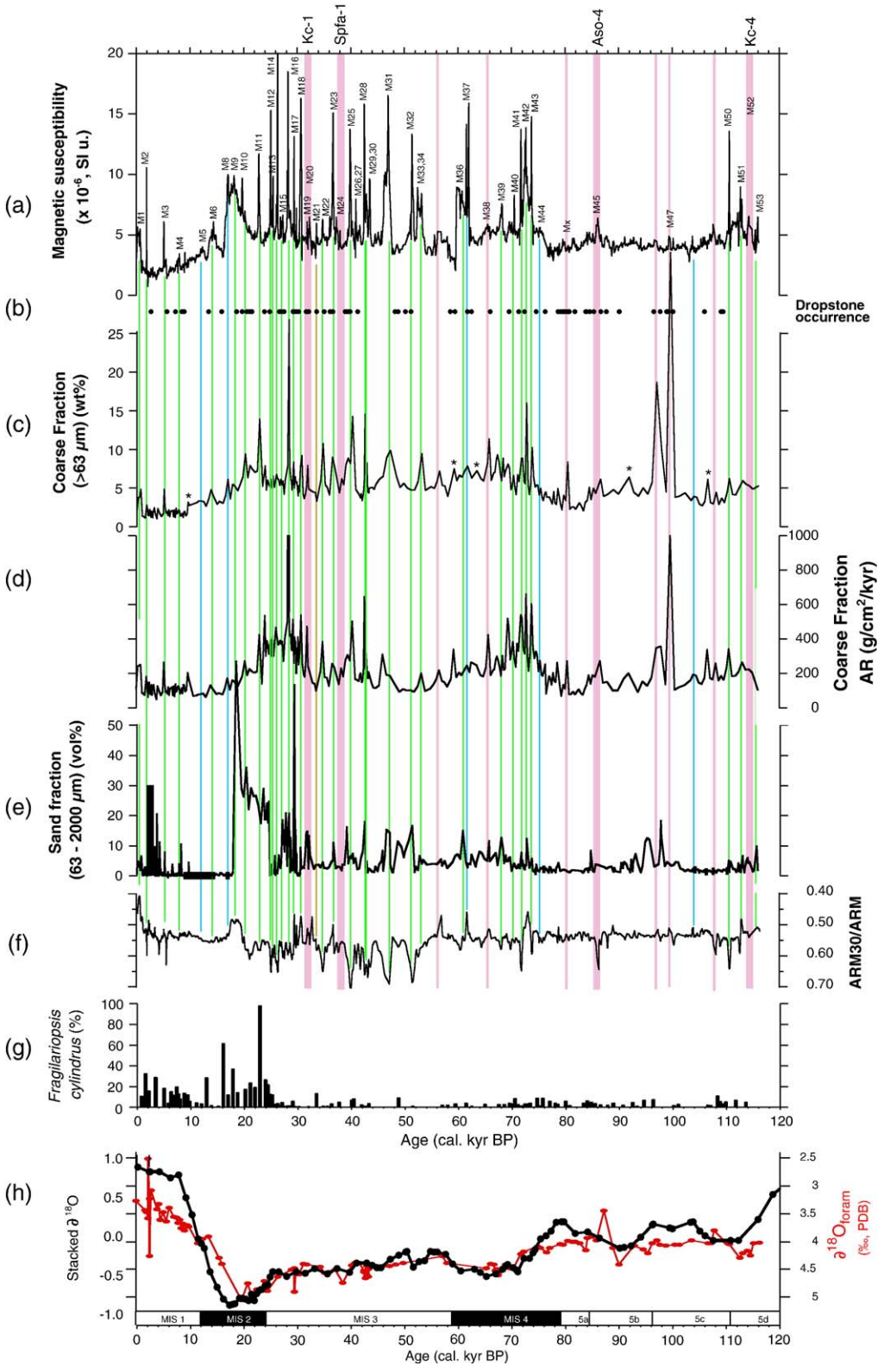
Kc-1
Spfa-1
Aso-4
Kc-4
(a)
Magnetic susceptibility (x 10⁻⁶, SI u.)
(b)
Dropstone occurrence
(c)
Coarse Fraction (>63 μm) (wt%)
(d)
Coarse Fraction AR (g/cm²/kyr)
(e)
Sand fraction (63 - 2000 μm) (vol%)
(f)
ARM30/ARM
(g)
Fragilariopsis cylindrus (%)
Age (cal. kyr BP)
(h)
Stacked ∂¹⁸O
∂¹⁸Oforam (‰, PDB)
MIS 1
MIS 2
MIS 3
MIS 4
5a
5b
5c
5d
Age (cal. kyr BP)

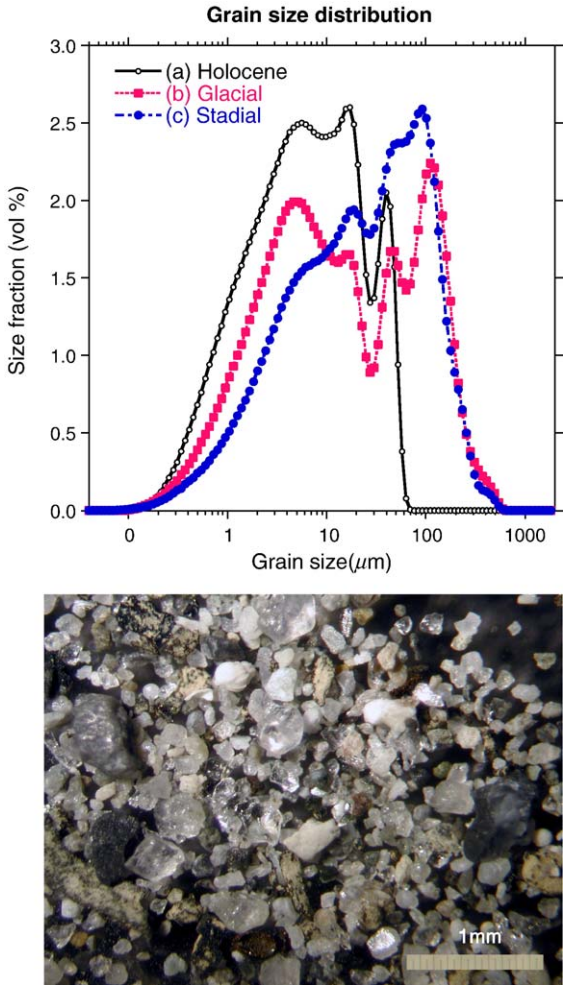


Fig. 6. Typical grain size distribution of terrigenous fraction. (a) Interglacial (Holocene) sample (Section 1, ID=9C, corrected depth 65.1–67.7 cm), (b) glacial sample (Section 10, ID=3C, corrected depth 1307.6–1310.1 cm), and (c) stadial sample (Section 31, ID=6C, corrected depth 4046.6–4049 cm). Obvious troughs in the grain size distribution of glacial sample were 28 and 63 μm in diameter. The grain size distribution of terrigenous fraction was measured with a laser diffraction grain size analyzer (Coulter LS230) after removing carbonate by acidification, organic matter with $H_2O_2$, and opal with $Na_2CO_3$ from aliquot samples. (d) Coarse fraction of glacial sample (Section 9, ID=9–19C, corrected depth 1275–1277.5 cm). The fraction was screened on 65-μm sieve without chemical treatments.

fraction were consistent with the relative abundance of diatom taxa, *Fragilariopsis cylindrus* and *Fragilariopsis oceanica* (Okazaki et al., 2005) in Core MD01-2412 (Fig. 5g). Relative abundances of *F. cylindrus* and *F. oceanica* showed a similar trend, with notable peaks during 15–30 ka (MIS2). Characteristically, both taxa are present within flowing ice or attached to its base in areas covered with sea-ice (Heiden and Kolbe, 1928; Gran and Braarud, 1935). *F. cylindrus* is one of a few bipolar species (Hasle, 1965), which is often found in pack-ice (Heiden and Kolbe, 1928). *F. oceanica* is a member of ice flora, in waters of − 1 to 3 °C (Hasle, 1965; Horner, 1976), which has identical distribution with *F. cylindrus* (Sancetta, 1982). Therefore, the sand fraction in the Core MD01-2412 is interpreted as ice-rafting debris.

Paleoceanographic condition obtained by IRD in particular area should be considered before using IRD as environmental proxy in the past. In perennial sea-ice conditions such as the Arctic Ocean, we cannot expect to find IRD during cold intervals because perennial sea-ice cannot release any debris to the bottom sediment. The occurrence of the IRD in the sediment core in modern perennial sea-ice areas represents melting of sea-ice condition during warm periods (Phillips and Grantz, 1997; Jakobsson et al., 2000). If the sediment contains no IRD in the perennial sea-ice area, it indicates a sea-ice condition in which IRD do not sink down from

the sea surface at the location of sediment core because sea-ice do not melt. In a seasonal sea-ice area, it might be expected perennial sea-ice condition during the glacial intervals. However, in the case of the Okhotsk Sea locating the lowest latitude in the northern hemisphere as seasonal sea-ice area, it has been seasonal sea-ice condition at least during the late Quaternary. Gorbarenko et al. (2003) reported that summer sea-ice melting and delivery of a significant amount of ice-rafted material were found during the glaciation in major part of Okhotsk Sea based on diatom and IRD analyses. They pointed out that only the far northwestern part of the sea was covered by sea-ice year round during the glaciation. Based on the present meteorological observation of the past 20 yrs from 1973 to 1993 (Tachibana et al., 1996), abrupt decrease of sea-ice cover over the southern part of the Okhotsk Sea occurred at the end of the 1980s owing to an abrupt changes in the weakening of the Aleutian low. The abrupt changes occurred with the rise of temperature around Japan. On the analogy from the present long-term observation, sea-ice retreats during warm regime, and vice versa. Because the spatial distribution of IRD content in surface sediments was closely corresponded to average sea-ice extent by the satellite imagery (Sakamoto et al., 2005), increase of the IRD in the sediment core during in the seasonal sea-ice area, therefore, represents as paleocenographic condition as expanding of sea-ice during cold condition in the meaning of wider, thicker, and/or longer sea-ice coverage in a year.

### *4.4. Past sea-ice history in the SW Okhotsk Sea*

IRD fraction increased during the glacial periods (MIS 2, 3, and 4) with large amplitude variation in millennial timescale. Sea-ice coverage expanded to its maximum in the last glacial maximum. There is a relatively small variation during the Holocene (MIS 1) and the last interglacial (MIS 5). The IRD is found not only during cold glacial periods but also during warm periods in the SW Okhotsk Sea during the past 115 kyr. It represents that the sea-ice should melt on a seasonal and/or annual scale. The SW Okhotsk Sea has not been perennial but seasonal sea-ice conditions during the past 115 kyr.

Increase of the IRD represents an increase of drifting sea-ice with longer duration of sea-ice. In the SW Okhotsk Sea, all of sea-ice is drifting sea-ice from the north through Off Sakhalin in the present day. The development of the Aleutian Low results in a strong wind field, creating a colder climate over the Okhotsk region and expanding the sea-ice cover in the Sea of Okhotsk (Kimura and Wakatsuchi, 1999). According to the present observations, sea-ice in the Okhotsk Sea would expand under strong wind fields. During 120 kyrs, an increase of relative average size and intensity of polar atmospheric circulation during the glacial periods were proposed by Mayewski et al. (1997). A possible reason of expanding sea-ice in the SW Okhotsk Sea would be strong wind fields under enhanced polar atmospheric circulation during glacial periods.

On the other hand, sea-ice also expanded during interglacials (MIS 1 and 5), indicated by short-lived peaks of sand-fraction IRD and magnetic susceptibility, when the polar circulation had not intensified. Ogi et al. (2001) found that the inter-annual variation of summer Amur discharge is strongly negatively correlated with the sea-ice extent in the following winter in time-serial meteorological datasets from 1965 to 1995. They concluded that the autumn sea surface condition is very effective for the sea-ice formation that follows. The summer and autumn Amur discharge brings warm water advection onto the surface water in the Okhotsk Sea, reducing the potential freezing in the following winter. This implies that sea-ice expansion is also affected by change of the Amur River discharge in longer time scale. Fluctuation of the Amur River discharge is one of a possible forcing for changing sea-ice expansion during the warm periods.

## 5. Summary and conclusions

The findings of the present study are as follows:

(1) Utilizing AMS $^{14}$C dating of planktonic foraminifer shells, oxygen–isotope stratigraphy for foraminifer calcite, and tephrochronology obtained an age model during 115 kys for MD01-2412. Tephras of Kc-1, -2/3 and -4, Aso-4, and Spfa-1 were identified in this study.
(2) Sea-ice expansion in the Okhotsk Sea during the past 115 kyr was reconstructed by the measurement of coarse sand fraction, dropstone, and magnetic susceptibility. The magnetic susceptibility variation expressed a relatively quantitative measurement of the total IRD in this area.
(3) The SW Okhotsk Sea has not had perennial but seasonal sea-ice conditions during the 115 kyr.
(4) Sea-ice fluctuated with large amplitudes during the glacials (MIS 2, 3, and 4) but with relatively small variation during the Holocene (MIS 1) and the last interglacial (MIS 5) with millennial-scale variation.

(5) The enhanced polar atmospheric circulation accelerated the large sea-ice expansion during the glacials (MIS 2, 3, and 4).
(6) During the interglacials (MIS 1 and 5), change of the Amur River discharge would be one of the possible factors for sea-ice expansion.

## Acknowledgements

We would like to express our appreciation to the crew and scientists onboard the IMAGES WEPAMA 2001 Cruise of the R/V *Marion Defresne*.

## References

Akagawa, M., 1977. Characteristics of oceanographic conditions in the Okhotsk Sea and meteorological conditions over the Far East in November. The Oceanographical Magazine 28, 33–45.

Alfulis, M.A., Martin, S., 1987. Satellite passive microwave studies of Sea of Okhotsk ice cover and its relation to oceanic processes, 1978–1982. Journal of Geophysical Research 92, 13013–13028.

Aoki, K., Arai, F., 2000. Late Quaternary tephrostratigraphy of marine core KH93-3, LM-8 off Sanriku, Japan. The Quaternary Research 39 (2), 107–120 (in Japanese).

Aota, M., 1975. Studies on the Soya Warm Currents. Teion Kagaku 33, 151–172 (in Japanese).

Aota, M., Kawamura, T., 1978. Observation of oceanographic condition in the Okhotsk Sea coast of Hokkaido in winter. Teion Kagaku 37, 93–105 (in Japanese).

Bard, E., Arnold, M., Hamelin, B., Tisnerat-Laborde, N., Cabioch, G., 1998. Radiocarbon calibration by means of mass spectrometric $^{230}$Th/$^{234}$U and $^{14}$C ages of corals: An updated database including samples from Barbados, Mururoa and Tahiti. Radiocarbon 40, 1085–1092.

Danhara, T., Yamashita, H., Kasuya, M., 1992. An improved system for measuring refractive index using the thermal immersion method. Quaternary International 13/14, 89–91.

Dansgaard, W., Johnsen, S.J., Clausen, H.B., Dahl-Jensen, D., Gundestrup, N.S., Hammer, C.U., Hvidberg, C.S., Steffensen, J.P., Sveinbjornsdottir, A.E., Jouzel, J., Bond, G., 1993. Evidence for general instability of past climate from a 250-kyr ice-core record. Nature 364, 218–220.

Froggatt, P.C., 1983. Toward a comprehensive upper Quaternary tephra and ignimbrite stratigraphy in New Zealand using electron microprobe analysis of glass shards. Quaternary Research 19, 188–200.

Gloerson, P., Champbell, W.J., Cavelieri, D.J., Comiso, C., Parkinson, C.L., Zwally, H.J., 1992. Arctic and Antarctic sea-ice, 1978–1987: Satellite passive-microwave observations and analysis. NASA Special Publication SP-511, 290.

Gorbarenko, S.A., Leskov, V.Yu., Artemova, A.V., Tiedemann, R., Boebow, N., Nuernberg, D., 2003. Ice cover of the Sea of Okhotsk during the last glaciation and Hocolece. Doklady Earth Sciences 389, 208–211.

Gran, H.H., Braarud, T., 1935. A quantitative study of the phytoplankton in the bay of Fundy and the Gulf of Maine. Journal of Biological Board Canada 2, 279–467.

Harada, N., Ahagon, N., Sakamoto, Uchida, M., Ikehara, M., Shibata, Y., 2006. Rapid fluctuation of alkenone temperature in the southwestern Okhotsk Sea during the past 120 kyr. Global and Planetary Change 53, 29–46. doi:10.1016/j.gloplacha.2006.01.010.

Hasle, G.R., 1965. Nitzschia and Fragilariopsis species studied in the light and electron microscopes. III. The genus Fragilariopsis. Noreke Vidensk-Akademi i Oslo Math.-Naturwiss. KI., Skr., n. ser, vol. 21, pp. 1–47.

Heiden, H., Kolbe, R.W., 1928. Die marinen Diatomeen der Deutschen Sübpolar-Expedition 1902–1903. Deutsche Sübpolar-Expedition 1901–1903 8, 447–715.

Horner, R., 1976. Sea ice organisms. Marine Biology Annual Review 14, 167–182.

Itoh, M., Ohshima, I.K., 2000. Seasonal variations of water masses and sea level in the southwestern part of the Okhotsk Sea. Journal of Oceanography 56, 643–654.

Itoh, M., Ohshima, I.K., Wakatsuchi, M., 2003. Distribution and formation of Okhotsk Sea Intermediate Water: An analysis of isopycnal climatological data. Journal of Geophysical Research 108 (C8), 3258. doi:10.1029/2002JC001590.

Jakobsson, M., Lovlie, R., Al-Hanbali, H., Arnold, E., Backman, J., Morth, M., 2000. Manganese and color cycles in Arctic Ocean sediments constrain Pleistocene chronology. Geology 28, 23–26.

Kanamatsu, T., Matsuo, K., 2003. Rock magnetic study of sediments from the Japan Trench, ODP Leg 186: implications for deformation of sediments. In: Suehiro, K., Sacks, I.S., Acton, G.D., Oda, M. (Eds.), Proceedings of the Ocean Drilling Program, Scientific Results 186, College Station, TX (Ocean Drilling Program), vol. 186SR-113, pp. 1–21.

Kato, S., Yamagata, K., Okumura, A., 1995. AMS-$^{14}$C dates of Late Quaternary tephra layers erupted from the Shikotsu and Kuttara volcanoes (in Japanese). The Quaternary Research 34 (4), 309–313.

Kawahata, H., Ohshima, H., Shimada, C., Oba, T., 2003. Terrestrial–oceanic environmental change in the southern Okhotsk sea during the Holocene. Quaternary International 108, 67–76.

Kitagawa, K., Masazawa, T., Nakamura, T., Matsumoto, E., 1993. A batch preparation method for graphite targets with low background for AMS $^{14}$C measurements. Radiocarbon 35 (2), 295–300.

Kimura, N., Wakatsuchi, M., 1999. Processes controlling the advance and retreat of sea-ice in the Sea of Okhotsk. Journal of Geophysical Research 104 (C5), 11137–11150.

Kitani, K., 1973. An oceanographic study of the Okhotsk Sea: Particularly in regard to cold waters. Bulletin Far Seas Fish, Research Laboratory 9, 45–77.

Kume, H., Shibata, Y., Tanaka, T., Yoneda, M., Kumamoto, Y., Morita, M., 1997. The AMS facility at the National Institute for Environmental Studies (NIES), Japan. Nuclear Instruments.

Kuzmin, Y.V., Burr, G.S., Timothy Jull, A.J., 2001. Radiocarbon reservoir correction ages in the Peter The Great Gulf, Sea of Japan, and eastern coast of the Kunashiri, southern Kuriles (Northwestern Pacific). Radiocarbon 43, 477–481.

Machida, H., Arai, F., 2003. Atlas of Tephra in and Around Japan. University of Tokyo Press. 336 pp.

Mahar, B.A., 1988. Magnetic fabric studies of samples from Hole 808C, Nankai Trough. In: Hill, I.A., Taira, A., Firth, J.V., et al. (Eds.), Proceedings of the Ocean Drilling Program, Scientific Results 131, College Station, TX (Ocean Drilling Program), pp. 301–310.

Martinson, D.G., Pisias, N.G., Hays, J.D., Imblie, J., Moore Jr., T.c., Shackleton, N.J., 1987. Age dating and the orbital theory of the ice ages: development of a high-resolution 0 to 3000,000-year chronostratigraphy. Quaternary Research 27, 1–29.

Matsuyama, M., Aota, M., Ogasawara, I., Matsuyama, S., 1999. Seasonal variation of Soya Current (in Japanese with English abstract). Umi no Kenkyu 8, 333–338.

Mayewski, P.A., Meeker, L.D., Twickler, M.S., Whitlow, S.I., Yang, Q., Lyons, W.B., Prentice, M., 1997. Major features and forcing of

high latitude northern hemisphere atmospheric circulation over the last 110,000 years. Journal of Geophysical Research 102 (C12), 26,345–26,366.

Mizuta, G., Fukamachi, Y., Ohshima, I.K., Wakatsuchi, M., 2003. Structure and Seasonal Variability of the East Sakhalin Current. Journal of Physical Oceanography 33, 2430–2445.

Moroshkin, K.V., 1966. Water Masses of the Sea of Okhotsk. U.S. Dep. Of Comm., vol. 43942. Joint Publ. Res. Serv, Washington, D.C. 98 pp.

Mortlock, R.A., Froelich, P.N., 1989. A sample method for the rapid determination of opal in pelagic marine sediments. Deep-Sea Research 36, 1415–1426.

Ogi, M., Tachibana, Y., Nishio, F., Danchenkov, M., 2001. Does the fresh water supply from the Amur River flowing into the Sea of Okhotsk affect sea ice formation? Journal of Meteorological Society of Japan 79 (1), 123–129.

Ohshima, I.K., Mizuta, G., Itoh, M., Fukamachi, Y., Watanabe, T., Nabae, Y., Suehiro, K., Wakatsuchi, M., 2001. Winter Oceanographic conditions in the Southwestern Part of the Okhotsk Sea and Their Relation to Sea Ice. Journal of Oceanography 57, 451–460.

Ohshima, I.K., Wakatsuchi, M., Fukamachi, M., Mizuta, Y., 2002. Near-surface circulation and tidal currents of the Okhotsk Sea observed with satellite-tracked drifters. Journal of Geophysical Research 107 (C11), 3195. doi:10.1029/2001JC001005.

Okazaki, Y., Takahashi, K., Katsuki, K., Ono, A., Hori, J., Sakamoto, T., Uchida, M., Shibata, Y., Ikehara, M., Aoki, A., 2005. Late Quaternary paleoceanographic changes in the southwestern Okhotsk Sea: Evidence from geochemical, radiolarian, and diatom records. Deep Sea Research II 52, 2332–2350. doi:10.1016/j.dsr2.2005.07.007.

Okumura, 1991. Quaternary tephra studies in the Hokkaido district, Northern Japan (in Japanese). The Quaternary Research 30 (5), 379–390.

Parkinson, C.L., Comiso, C., Zwally, H.J., Cavelieri, D.J., Gloerson, P., Champbell, W.J., 1987. Arctic sea-ice, 1973–1976: Satellite passive-microwave observations. NASA Spec. Pub, vol. SP-489. 296 pp.

Pearson, A., McNichol, A.P., Schneider, R.J., Von Reden, KF., 1998. Microscale AMS $^{14}$C measurement at NOSAMS. Radiocarbon 40 (1), 161–175.

Phillips, R.L., Grantz, A., 1997. Quaternary history of sea ice and paleoclimate in the Amerasia basin, Arctic Ocean, as recorded in the cyclical strata of Northwind Ridge. Geologocal Society of America Bulletin 109, 1101–1115.

Sakamoto, T., Ikehara, M., Aoki, K., Iijima, K., Kimura, N., Nakatsuka, T., Wakatsuchi, M., 2005. Ice-rafted debris (IRD)-based sea-ice expansion events during the past 100 kyrs in the Okhotsk Sea. Deep Sea Research II 52, 2275–2301. doi:10.1016/j.dsr2.2005.08.007.

Sancetta, C., 1982. Distribution of diatom species in surface sediment of the Bering and Okhotsk Seas. Micropaleontology 28, 221–257.

Steiget, E.J., Grootes, P.M., Stuiver, M., 1994. Seasonal precipitation timing and ice core records. Science 266, 1885–1886.

Stuiver, M., Grootes, P.M., Braziunas, T.F., 1995. The GISP2 $^{18}$O climate record of the past 16,500 years and the role of the sun, ocean and volcanoes. Quaternary Research 44, 341–354.

Stuiver, M., Reimer, P.J., Bard, E., Beck, J.W., Burr, G.S., Hughen, K.A., Kromer, B., McCormac, G., van der Plicht, J., Spurk, M., 1998. INTCAL98 radiocarbon age calibration, 24,000–0 cal BP. Radiocarbon 40, 1041–1083.

Széréméta, N., Bassinot, F., Balut, Y., Labeyrie, L., Pagel, M., 2004. Oversampling of sedimentary series collected by giant piston corer. Evidence and corrections based on 3.5-kHz chirp profiles. Paleoceanography 19 (1). doi:10.1029/2002PA000795.

Tachibana, Y., Honda, M., Takeuchi, K., 1996. The abrupt decrease of the sea ice over the southern part of the Sea of Okhotsk in 1989 and its relation to the recent weakening of the Aleutian low. Journal of the Meteorological Society of Japan 74 (4), 579–584.

Takahashi, K., Soeda, Y., Izuho, M., Aoki, K., Yamada, G., Akamatsu, T., 2004. A new specimen of *Palaeoloxodon naumanni* from Hokkaido and its significance (in Japanese). The Quaternary Research 43, 169–180.

Takizawa, T., 1982. Characteristics of the Soya Warm Current in the Okhotsk Sea. Journal of Oceanography of the Society of Japan 38, 281–292.

Talley, L.D., 1991. An Okhotsk Sea water anomaly: implications for ventilation in the North Pacific. Deep Sea Research 38, 171–190.

Tanaka, A., Yoneda, M., Uchida, M., Shibata, Y., Uehiro, T., Morita, M., 2000. Recent advances in $^{14}$C measurement at NIES-TERRA. Nuclear Instruments and Methods in Physics Research. Section B 172, 107–111.

Toyota, T., Kawamura, T., Wakatsuchi, M., 2000. Heat budget in the ice cover of the southern Okhotsk Sea. Journal of the Meteorological Society of Japan 78 (5), 585–596.

Uchida, M., Shibata, Y., Kawamura, K., Kumamoto, Y., Yoneda, M., Ohkushi, K., Harada, N., Hirota, M., Mukai, H., Tanaka, A., Kusakabe, M., Morita, M., 2001. Compound-specific radiocarbon ages of fatty acids from bathyal sediments in the western North Pacific. Radiocarbon 43, 949–956.

Uchida, M., Shibata, Y., Yoneda, M., Kobayashi, T., Morita, M., 2004. Technical progress in AMS microscale radiocarbon analysis. Nuclear Instruments and Methods in Physics Research-B 223–224, 313–317.

Wakatsuchi, M., Martin, S., 1991. Water circulation in the Kuril Basin of the Okhotsk Sea and its relation to eddy formation. Journal of Oceanography of the Society of Japan 47, 152–168.

Watanabe, T., 1963. On the reinforcement of the East Sakhalin Current preceding to the Sea Ice season off the coarst of Hokkaido—study on sea ice in the Sea of Okhotsk (IV). The Oceanographical Magazine 14 (2), 117–130.

Watanabe, T., Wakatsuchi, M., 1998. Formation of 26.8–26.9 $\sigma\tau$ water in the Kuril Basin of the Sea of Okhotsk as possible origin of North Pacific Intermediate Water. Journal of Geophysical Research 103, 2849–2865.

White, J.W.C., Barlow, L.K., Fisher, D., Grootes, P.M., Jouzel, J., Johnsen, S.J., Stuiver, M., Clausen, H.B., 1997. The climate signal in the stable isotopes of snow from Summit, Greenland: Results of comparisons with modern climate observations. Journal of Geophysical Research 102, 26425–26439.

Yanagida, M., 1994. Age of the Shikotsu Pumice Fall-1 deposit (in Japanese). The Quaternary Research 33 (3), 205–207.

Yokoyama, Yamashita, 1986. Preliminary measurement of refractive index for orthorhombic pyroxene and hornblendes by a new refractometer (RIMS-86). Tsukumo Chigaku 21, 30–36 (in Japanese).